Title	Electrical properties of platinum interconnects deposited by electron beam induced deposition of the carbon-free precursor, Pt(PF3)4
Authors	O'Regan, Colm;Lee, Angelica;Holmes, Justin D.;Petkov, Nikolay;Trompenaars, Piet;Mulders, Hans
Publication date	2013-03
Original Citation	O'REGAN, C., LEE, A., HOLMES, J. D., PETKOV, N., TROMPENAARS, P. & MULDERS, H. 2013. Electrical properties of platinum interconnects deposited by electron beam induced deposition of the carbon-free precursor, Pt(PF3)4. Journal of Vacuum Science & Technology B, 31, 021807. doi: 10.1116/1.4794343
Type of publication	Article (peer-reviewed)
Link to publisher's version	http://scitation.aip.org/content/avs/journal/jvstb/31/2/10.1116/1.4794343 - 10.1116/1.4794343
Rights	© 2013 American Vacuum Society. All rights reserved.
Download date	2024-04-27 20:25:34
Item downloaded from	https://hdl.handle.net/10468/2795

Electrical properties of platinum interconnects deposited by electron beam induced deposition of the carbon-free precursor, $Pt(PF_3)_4$

Colm O'Regan, Angelica Lee, Justin D. Holmes, and Nikolay Petkov[a)]
Materials Chemistry and Analysis Group, Department of Chemistry and the Tyndall National Institute, University College Cork, Cork, Ireland and Centre for Research on Adaptive Nanostructures and Nanodevices (CRANN), Trinity College Dublin, Dublin 2, Ireland

Piet Trompenaars and Hans Mulders
FEI Electron Optics, Achtseweg Noord 5 5651 GG Eindhoven, The Netherlands

(Received 19 December 2012; accepted 21 February 2013; published 4 March 2013)

Comprehensive analysis of the electrical properties, structure and composition of Pt interconnects, developed via mask-less, electron beam induced deposition of the carbon-free Pt precursor, $Pt(PF_3)_4$, is presented. The results demonstrate significantly improved electrical performance in comparison with that generated from the standard organometallic precursor, $(CH_3)_3Pt(C_pCH_3)$. In particular, the Pt interconnects exhibited perfect ohmic behavior and resistivity that can be diminished to 0.24×10^{-3} Ω cm, which is only one order of magnitude higher than bulk Pt, in comparison to 0.2 Ω cm for the standard carbon-containing interconnects. A maximum current density of 1.87×10^7 A cm^{-2} was achieved for the carbon-free Pt, compared to 9.44×10^5 A cm^{-2} for the standard Pt precursor. The enhanced electrical properties of the as-deposited materials can be explained by the absence of large amounts of carbon impurities, and their further improvement by postdeposition annealing in N_2. *In-situ* TEM heating experiments confirmed that the annealing step induces sintering of the Pt nanocrystals and improved crystallinity, which contributes to the enhanced electrical performance. Alternative annealing under reducing conditions resulted in improved performance of the standard Pt interconnects, while the carbon-free deposit suffered electrical and structural breakage due to formation of larger Pt islands. © *2013 American Vacuum Society*. [http://dx.doi.org/10.1116/1.4794343]

I. INTRODUCTION

Reports thus far have made extensive use of lithographic, resist-based methods such as optical or electron beam lithography followed by metal evaporation and lift-off to make electrical contacts to semiconducting nanowires[1–3] and nanotubes,[4] allowing single nanowire or nanotube devices such as field-effect-transistors,[5,6] nanoelectromechanical systems,[7–10] and chemical sensors[11] to be demonstrated. Although successful, the process of contact definition to nanowires by metal evaporation through a lithography mask tends to be very time-consuming, with many processing steps, and normally is not applicable to fragile or flexible substrates. For rapid and flexible prototyping of single nanowire or nanotube based devices on a diverse range of substrates, direct-writing of electrical contacts via maskless methods is more practical and poses significant advantages.[12]

Among direct write techniques for metal-containing interconnects such as laser direct write and others,[13] the methods based on using scanning focused electron or ion beam deposition offer necessary nanometer resolution and precision for contacting nanowires and nanotubes. Briefly, a gaseous precursor, typically organometallic, is injected into the chamber where a focused ion or electron beam is used to decompose the precursor into volatile and nonvolatile species. The nonvolatile species are deposited while the volatile species are pumped away into the vacuum chamber.[14] The decomposition process is a result of the interaction of surface emitted secondary electrons in the irradiated area with locally adsorbed gas molecules delivered by a gas injector system (GIS). As a result, using either electron beam induced deposition (EBID)[15,16] or ion beam induced deposition (IBID),[17–20] nanowire interconnects can be deposited in a single step, making it a very facile process. Furthermore, the technique has the potential to surpass the resolution limits posed by top–down lithographic methods.[21] The IBID and EBID processes have so far been used to deposit metal-containing contacts on Si (Refs. 22 and 23), ZnO,[24] GaN,[25] and Ge (Ref. 26) nanowires and carbon nanotubes.[4] Generally, the EBID process has the advantage of being less damaging for the underlying materials in comparison to the IBID process.

Unfortunately, a major disadvantage of the EBID developed metal-containing interconnects is that the metal-containing deposits are highly resistive. The standard Pt precursor used in dual-beam FIB systems is the organometallic trimethyl(methylcyclopentadienyl)platinum(IV), $(CH_3)_3Pt(C_pCH_3)$. This precursor is used for Pt layers on TEM samples being prepared for cross-sections in order to protect the sample from the damaging ion beam.[27] However, when the same precursor is used to develop interconnects, the result is a highly resistive deposit. This is due to the high carbon content, with reports quoting a carbon content as high as 80%.[28] Therefore, the interconnects suffer a deterioration in resistivity, which can be up to 5 orders of magnitude higher than the resistivity of pure bulk Pt (10.6×10^{-6} Ω cm). More importantly, the reported resistivity values vary significantly from one report to another, having a variation of at least several orders of magnitude. The lowest reported resistivity value

[a)]Electronic mail: nikolay.petkov@tyndall.ie

for Pt interconnects deposited by using the standard $(CH_3)_3Pt(C_pCH_3)$ precursor is 1.4 ($\pm$0.2) $\times 10^{-2}$ Ω cm and it is obtained after thermal annealing of the material.[15]

A useful alternative to the organometallic based precursor is tetrakis (trifluorophosphine) platinum, $Pt(PF_3)_4$. This is a carbon-free liquid precursor, which has not been studied in great detail until now. The carbon-free structure means that no carbon from the precursor will contribute to carbon contained in the deposits, thus minimizing carbon content while improving overall performance. While studies of the electron scattering,[29] annealing,[28] and structure[30] of $Pt(PF_3)_4$ have been reported previously, comprehensive studies on the electrical properties of interconnects deposited using this precursor have not. The first reported resistivity values demonstrated the immediate advantage of using this carbon-free precursor for the EBID of Pt material. Resistivity values are at least one or two orders of magnitude lower (lowest resistivity reported is at 6.9×10^{-4} Ω cm) than the lowest reported values for the $(CH_3)_3Pt(C_pCH_3)$ precursor.[31] Similarly to the $(CH_3)_3Pt(C_pCH_3)$ deposits, it is postulated that these values can be further lowered by thermal annealing, though such studies have yet to be carried out.

Herein, we report on a comprehensive study of the electrical performance and thermal evolution of individual Pt interconnects deposited using EBID of $Pt(PF_3)_4$. The improved properties of the carbon-free deposits in terms of higher breakdown currents and lower resistivity are comprehensively compared and contrasted to the ones obtained from the standard organometallic precursor. The influence of two different thermal treatment processes over the electrical and structural properties of both types of Pt interconnects were studied. Advanced electron microscopy methods such as high angle annular dark field (HAADF) imaging coupled with electron energy loss spectroscopy (EELS) measurements of device cross-sections complement the electrical analysis data by identifying the impurities of the deposition process. Additionally, *in-situ* TEM annealing studies of the deposits on electron transparent membranes revealed the dynamics of the postdeposition thermal treatment and highlighted the key structural changes responsible for the improved electrical performance of the interconnects.

II. EXPERIMENT

All Pt interconnect depositions were performed on a FEI Helios NanoLab^{TM} Dual-Beam instrument using an acceleration voltage of 5 kV. Deposition dwell time was set at 5.0 μs with a multipass serpentine scan type and the distance from the GIS to the sample was 200 μm for all depositions. The pixel distance spacing was 11.54 nm for the $Pt(PF_3)_4$ precursor and 23.07 nm for the $(CH_3)_3Pt(C_pCH_3)$ precursor. The sample substrate (with prefabricated Au/Ni contact pads) was placed in the chamber along with a Faraday cup in order to measure the exact beam current from the electron source. Nominal beam currents were set at 1.4 nA, while the actual mean current measured using the Faraday cup was 1.28 ± 0.09 nA. The instrument was then evacuated overnight giving a chamber pressure of about 6.0×10^{-7} mbar. Upon opening the GIS, the pressure in the chamber increased an order of magnitude higher than the base pressure, suggesting a sufficient quantity of precursor was injected into the system. After closing the GIS, the pressure returned to its original value within 10 min. EBID was applied by a tetrakis (trifluorophosphine) platinum ($Pt[PF_3]_4$) GIS [CAS number: 19529-53-4, vapour pressure 240 mm (55 °C), boiling point 80 °C, MW 547.01, supplied by STREM Chemicals Inc.] and a standard $(CH_3)_3Pt(C_PCH_3)$ GIS to selectively deposit Pt metal onto Au/Ni contact pads for 2- and 4-point electrical measurements. It should be noted that for the rest of the discussion, we refer to $Pt(PF_3)_4$ as the carbon-free Pt and the $(CH_3)_3Pt(C_PCH_3)$ as standard Pt. Interconnects with nominal dimensions of 30 μm $\times$ 200 nm and thicknesses of approximately 20 nm were deposited. Annealing was achieved by rapid thermal annealing at 400 °C for 1 min in N_2 and in forming gas (5% H_2 in N_2), respectively. The ramp time from room temperature to 400 °C was achieved in 2 min giving a rate of approximately 3.3 °C s^{-1}. Cross-sectional TEM studies were performed on a JEOL JEM 2100 transmission electron microscope equipped with Gatan *in-situ* heating stage. STEM and EELS analyses were performed using JEOL 2010F microscope equipped with Gatan GIF camera.

The electrical measurements were performed using a Cascade Microtech probe station with a B1500 (Agilent Technologies) semiconductor device analyser. All scanning electron microscopy (SEM) images were taken on a FEI Helios NanoLab. TEM cross-sections were performed using the standard FIB lift-out technique described elsewhere.[32]

III. RESULTS AND DISCUSSION

A. Pt interconnect deposition and electrical characterization

Before developing Pt interconnect lines, the performance of the GIS and corresponding deposition rates was monitored by developing 1 μm^2 square patterns at 5 kV and varying beam currents at constant deposition times as described in our previous report.[33] These results were used to estimate the thickness of the deposits and to calibrate the time needed to obtain the desired thickness of the Pt lines. Figure 1(a) shows *I-V* curves for two devices, prepared using carbon-free and standard Pt precursors with their corresponding SEM images, used to measure the electrical performance of the interconnects. The Pt interconnects were deposited on the same substrate under identical conditions (base pressure and beam current). Initial electrical characterization was carried out on as-prepared devices. Initially, the devices were measured in a four-point configuration to determine if there was any contact resistance contributions coming from the Pt-Au electrode contacts. For these measurements, a current is forced between two outer terminals while the potential drop between the two inner terminals is measured, enabling separation of the wire (interconnect) resistance R_{wire} from the contact resistance $R_{contact}$. Contact resistance values were obtained by comparing the resistance values obtained from the 2- and 4-probe measurements, where the 2-probe

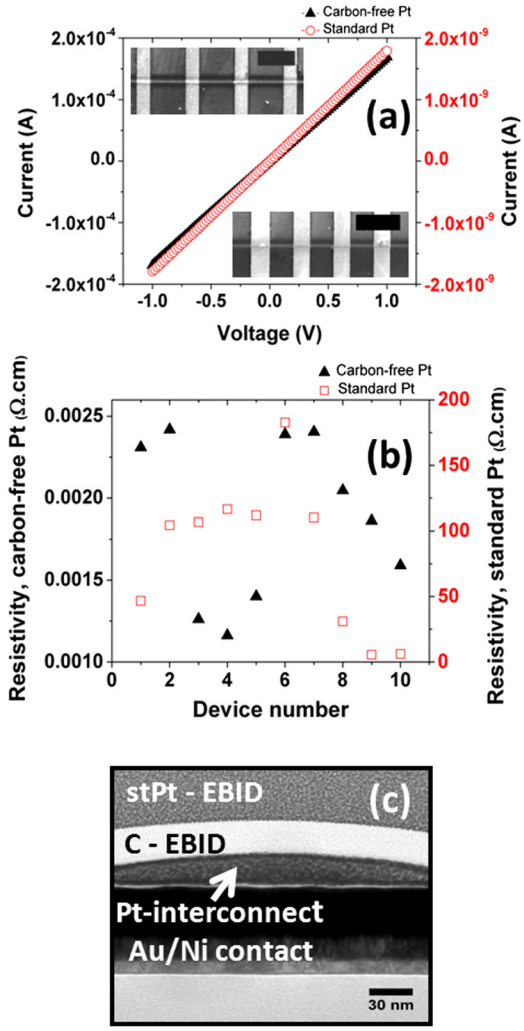

FIG. 1. (Color online) Room temperature electrical measurements of carbon-free and standard Pt interconnects. (a) 2-point I-V curves for a Pt interconnect deposited using the $Pt(PF_3)_4$ precursor and $(CH_3)_3Pt(C_PCH_3)$ precursor. The left (black) y-axis corresponds to the carbon-free Pt while the right (red) y-axis corresponds to the standard Pt. Insets are SEM images of the carbon-free Pt (top) and standard Pt (bottom) interconnects deposited across four Au/Ni contact pads. Scale bar in both is 5 μm. (b) Scatter plot showing the distribution of resistivities calculated for several devices deposited under identical conditions. Right hand (red) y-axis corresponds to standard Pt and the left hand (black) y-axis corresponds to the carbon-free Pt. (c) TEM cross-section micrograph of a carbon-free Pt interconnect. Scale bar is 30 nm. stPt-EBID is standard Pt–electron beam induced deposition. C-EBID is carbon-electron beam induced deposition.

measurements allow the total resistance between the 2 inner terminals ($R_{2\text{-probe}}$) to be determined while the 4-probe set-up allows the resistance of the Pt interconnect between the inner terminals ($R_{4\text{-probe}}$) to be obtained. The contact resistance (R_{contact}) can then be calculated from Eq. (1): $2R_{\text{contact}} + R_{4\text{-probe}} = R_{2\text{-probe}}$.[20] The difference in slope between the 2- and 4-point measurements is due to the contact resistance. However, as can be seen in Fig. S1 in the supporting information,[34] the slopes are almost identical, suggesting that the contact resistance is negligible (assumed to be less than 100 Ω) compared to the Pt wire resistance (5.0 kΩ) and does not contribute to a significant fraction of the total resistance. As a result, 2-point measurements were used in the rest of the study. For the two-point measurement configuration, a voltage was applied between the two inner contacts as the current flowing through them was measured. As can be seen in Fig. 1(a), the room temperature current–voltage (I-V) plots of both carbon and standard Pt deposits exhibited well defined linear regimes up to 1 V, suggesting that the wire-electrode contacts were ohmic.

Figure 1(b) shows a scatter plot which illustrates the distribution of resistivities of both the standard and carbon-free Pt depositions (10 devices from each precursor are represented). The resistivities for the carbon-free Pt interconnects ranged from 1.2×10^{-3} to 2.4×10^{-3} Ω cm, suggesting a very high reproducibility for this specific precursor. However, the resistivities obtained for the standard Pt precursor are less consistent, ranging between 1 and 180 Ω cm. The mean resistivity ($1.88 \pm 0.5 \times 10^{-3}$ Ω cm) obtained for interconnects produced using the carbon-free Pt precursor is still about two orders of magnitude higher than that of bulk Pt, but almost 4 orders of magnitude lower than the obtained mean resistivity of standard Pt (82.12 ± 57.35 Ω cm). This enormous difference in resistivity confirms the advantage of using the carbon-free $Pt(PF_3)_4$ as a precursor for the EBID of Pt in a dual-beam FIB system. Overall, these results are not surprising and reflect our previous study where we show that the deposits obtained using the carbon-free Pt precursor are composed of a continuous network of polycrystalline Pt nanoparticles embedded in amorphous matrix.[33] A detailed investigation of the composition of these structures by HAADF imaging and EELS spectral imaging is given below.

The cross-sections of the individual interconnects were obtained via cross-sectional TEM imaging, as shown Fig. 1(c). These cross-sections provided important information regarding the structure of the Pt wires. It is clearly shown that the structures have no sharp edges and that the overall cross-section is not rectangular, a factor which affects the overall calculated resistivity ($\rho = R \times A/L$, where ρ is the resistivity, R is the resistance, A is the cross-sectional area, and L is the channel length between the two inner terminals). The nominal cross-sectional area, used in the majority of the reports to calculate the resistivity of a metal-containing interconnect developed by EBID, is much smaller than the one observed by TEM cross-sections due to increased width of the deposit (Fig. S2, supporting information[34]), thus underestimating the calculated resistivity. For example, the nominal cross-section of our deposits is set at 4000 nm^2, whereas the "true" area of the cross-sectioned Pt line used in the calculations above and seen by TEM is almost 6000 nm^2. If we use the nominal cross-section area of the interconnect to calculate the resistivity, this will decrease the calculated resistivity for the best performing device (1.2×10^{-3} Ω cm) to 0.8×10^{-3} Ω cm, which compares favorably to the already reported value of 0.69×10^{-3} Ω cm.[31]

In this study, a relatively low beam current of ~1.4 nA allows adequate decomposition of the Pt precursor over a time period of approximately 3 min, which compares favorably to the very high currents used by Ervin and coworkers (13–46 nA) to decompose the same precursor.[35] While deposition times can be reduced at high beam

currents, beam sensitive samples may suffer beam damage resulting in higher resistivities. The only varying parameter in our experiments during deposition was the fluctuating residual gas in the vacuum chamber, which should be kept to a minimum to ensure reproducible results and to minimize contamination of the deposited Pt structures. A chamber pressure of 6.0×10^{-7} mbar was achieved prior to Pt deposition at all times, to minimize contamination from residual gas in the chamber.

In order to further explore the interconnects formed from the carbon-free Pt precursor as possible interconnects for nanowire devices, we carried out maximum current density (J_{max}) measurements using a 2-terminal set-up on individual interconnects and compared the results with those obtained for standard Pt, as shown in Fig. 2(a). Our measurements show that a single interconnect can carry a current of approximately 1.1 mA before electrical breakdown, compared to 0.11 mA for the standard Pt, corresponding to a maximum current density of 1.87×10^{7} A cm^{-2} for the carbon-free Pt and 9.44×10^{5} A cm^{-2} for the standard Pt. J_{max} for interconnects formed from the carbon-free Pt is two orders of magnitude higher than those formed from the standard Pt precursor, confirming the superiority of $Pt(PF_3)_4$ as a candidate for Pt interconnect formation. Figure 2(b) shows an SEM image of a failed interconnect where the point of electrical breakdown occurs consistently between electrodes two and three (closer to one than the other) where you would expect to find the least heat dissipation and highest temperature due to Joule heating.[36,37] Additionally, this fact serves as an indirect indication that the Pt deposition at the edges of the Au/Ni contact lines is conformal, and does not form sharp steps and breakages (often seen for the metal evaporation process) that can result in higher resistivity of the interconnects.

B. Annealing studies on deposited Pt

Figure 3(a) shows I-V measurements for a standard Pt interconnect before and after annealing at 400 °C under nitrogen gas for 1 min. Before annealing, the I-V plot (black) displays perfect ohmic behavior with a resistivity of 115 Ω cm. After annealing, the Pt interconnect demonstrates a resistivity of 93.4 Ω cm. This small decrease in resistivity is possibly due to particles sintering together and a decrease in the impurities content. Previously, annealing in an oxidative atmosphere has been used to purify standard Pt interconnects.[15] This type of a treatment showed decreased interconnect resistivity of about two orders of magnitude in comparison to the as-deposited material but still much higher than bulk Pt, most probably, due to surface oxidation. In contrast to this, N_2 annealed carbon-free Pt demonstrates a much larger decrease in resistance (about 5 times) when

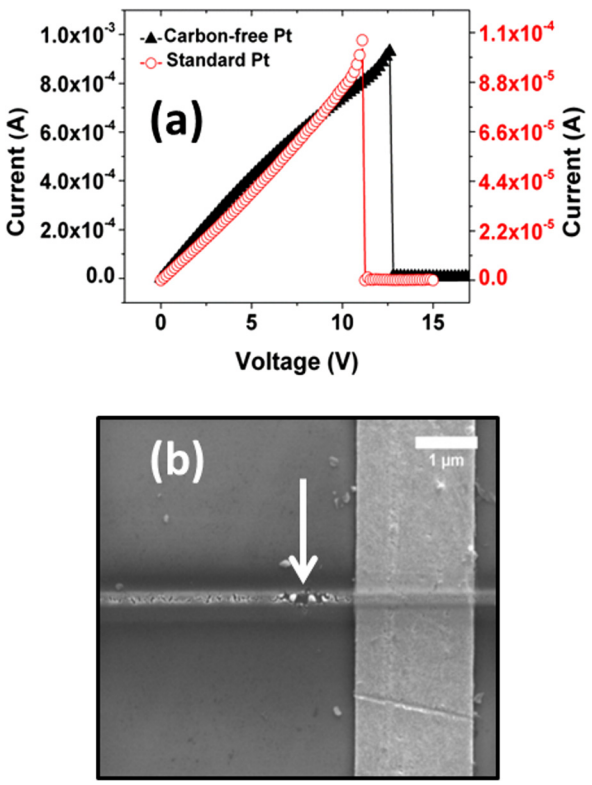

FIG. 2. (Color online) Electrical transport measurements performed on carbon-free and standard Pt interconnects. (a) I-V measurements recorded at higher applied voltages for standard Pt (open red circles) and carbon-free Pt (solid black triangles) interconnects. The rapid drop in current around 12 V for both interconnects is due to electrical breakdown of the wire. (b) SEM image showing the point of breakdown of the wire between the two inner electrodes. Scale bar is 1 μm.

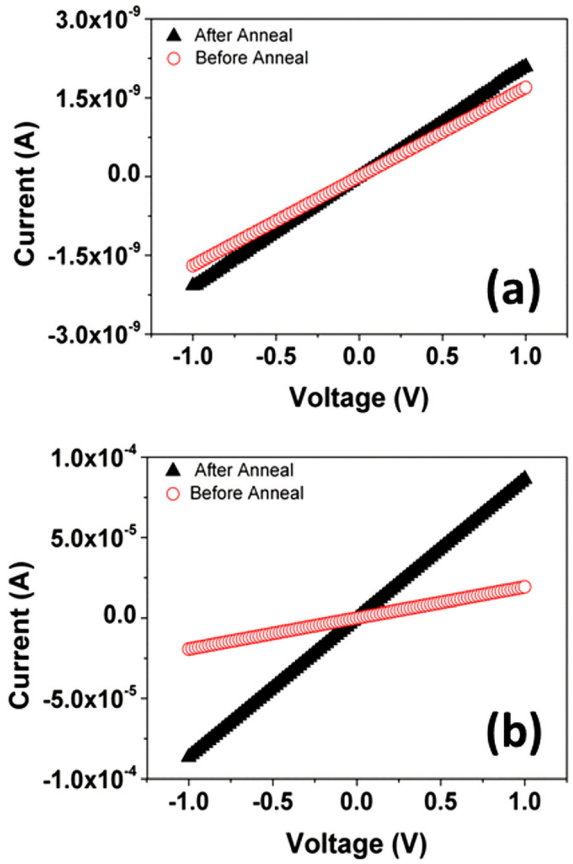

FIG. 3. (Color online) I-V measurements of Pt interconnects before and after annealing. (a) I-V curve for a standard Pt interconnect before and after annealing under nitrogen for 1 min. (b) I-V curve for carbon-free Pt interconnect before and after annealing under nitrogen for 1 min.

compared to the preannealed sample [Fig. 3(b)]. This translates into a similar decrease in the resistivity. Taking into account the calculated resistivity using the "true" cross-sectional area of the best performing untreated sample (1.2×10^{-3} Ω cm), the N_2 annealed analogue will show a resistivity of 0.24×10^{-3} Ω cm. If we use the nominal cross-sectional area in calculating the resistivity, this will further decrease the value to 0.16×10^{-3} Ω cm, which is only one order of magnitude higher than bulk Pt and to the best of our knowledge, the lowest reported resistivity for Pt developed by EBID.

To explore the effect of a reducing environment on thermal treatment of both types of Pt interconnects, rapid thermal annealing under forming gas was performed at 400 °C for 1 min. Figure S3(a),[34] in the supplementary information, shows I-V measurements for a standard Pt interconnect before and after the forming gas anneal. In comparison to the pure N_2 anneals, annealing in the reducing atmosphere introduced changes in the interconnect that decreased the resistivity by about 2 orders of magnitude. Before annealing, the interconnect demonstrated a resistivity of 19.5 Ω cm, while after annealing there is a resistivity of 0.2 Ω cm. This value is one order of magnitude higher than the best reported resistivity for the standard Pt precursor[15] but is still among the lowest values reported. In comparison, the Pt interconnect developed by the carbon-free precursor showing a resistivity of about 1.2×10^{-3} Ω cm before the forming gas annealing, after thermal treatment showed almost no current flow (picoamps range). Additionally, the interconnect demonstrated electrical behavior that departs severely from typical ohmic I-V behavior (Fig. S3(b)[34]] from the supporting information). These drastically different results can be explained by looking at the integrity of both types of interconnects after annealing. The structure of the Pt interconnects developed by the standard precursor remained smooth and intact on the electrodes [inset in Fig. S3(a)[34]]. TEM images show that the overall volume remains the same, even though an increase of the overall Pt particle size is seen. In comparison, the SEM image of the carbon-free Pt interconnect after the forming gas anneal shows that the body of the interconnect is disjointed and broken into separate metal islands. The reason why the carbon-free interconnects broke apart during the forming gas anneal and the standard Pt deposits remained intact can be explained by the dissimilar composition and internal nanostructure of both materials that followed different transformation routes upon forming gas annealing. Normally, when heated under reducing conditions, thin films of noble metals form larger well-faceted and well-crystalline metal nanocrystals in contrast to the materials thermally treated under inert conditions.[38] Evidently, this type of process is happening to a greater extent for the carbon-free deposits. One explanation for this behavior is that the carbon-free deposits exhibit no amorphous interwoven carbon matrix surrounding the nanoparticles that can keep the structural integrity of the material and at the same time prevent the formation of larger crystallites. Additionally, previous studies in the literature[31] and our elemental analysis studies (shown below) show that the deposits encompass large phosphorous-containing clusters, which may accelerate the process causing the rest of the structure to break apart. Milder thermal conditions and deposits with minimized phosphorous content might result in preserving the structural integrity of the $Pt(PF_3)_4$ interconnects under forming gas annealing. In comparison, the organometallic Pt deposits are experiencing large improvements in the crystallinty resulting in enhanced electrical performance while the structural integrity is preserved by the surrounding amorphous carbon matrix. We postulate that a valuable route for further enhancement of the electrical performance of the standard Pt deposits can be a two-step annealing process where mild oxidative conditions are used to purify the deposits (decrease the carbon-content), which should be followed by annealing in reducing conditions to improve the grain size and crystallinity of the Pt framework. This two-step procedure is currently under investigation in our group. However, as the work is in its early stages, no significant results have yet been obtained and consequently have not been presented in this article. Such an investigation is of significant value due to the impressive electrical results obtained thus far and any further enhancement of the electrical performance of carbon-free depositions is highly desirable. Despite this, the two-step procedure would require significant additional experimentation and is therefore beyond the scope of this article.

As demonstrated previously, the electrical performance of the developed interconnects is a paramount function of the nanoscale structure and composition of the Pt deposits. We and others reported previously that the carbon-free material deposited via EBID is composed of nanocrystalline Pt particles and an amorphous matrix surrounding the nanoparticles. In order to determine the detailed elemental composition of the interconnects formed from the carbon-free Pt precursor, cross-sections of the Pt wires were obtained and examined by STEM imaging and line-scan EELS analysis [Figs. 4(a) and 4(b)]. Line-scan EELS data presented in Fig. 4(b) depicts the spatial distribution of the elements in a cross-section of a carbon-free Pt deposit before annealing. The elemental content averaged from the signals obtained across the whole section of the deposit are as follows: 61% Pt, 14% P, 15% O, and 10% C. The inclusion of phosphorous in the deposits has already been observed in the form of amorphous material, forming islands of increased phosphorous content along the length of the deposits.[35] Here, we observe that such islands are formed closer to the bottom of the deposits as seen on Fig. 4(b), with elemental content increasing to 20%. Interestingly, the oxygen profile follows the same trend, reaching 23% close to the bottom of the deposit. The Pt content is almost constant across the deposit, while carbon content is diminished in the region of higher phosphorous and oxygen content. The origin of the carbon and oxygen inclusion in the deposits cannot be a result of the decomposition of the carbon-free precursor molecules. There are several routes for carbon and oxygen incorporation, e.g., (i) from the residual gases in the microscope chamber as the electron beam is scanned during the deposition process, or (ii) from the residual gases during the elemental analysis itself. The latter will be extremely prominent

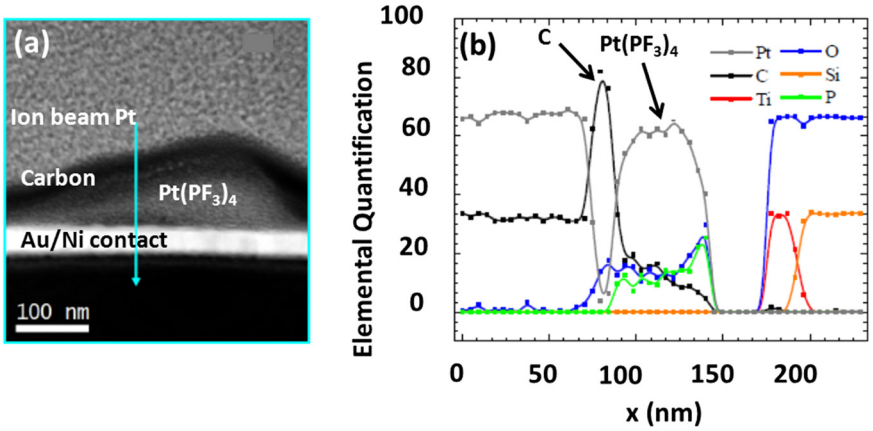

FIG. 4. (Color online) Cross-sectional TEM micrograph and EELS analysis of carbon-free interconnect. (a) Low-resolution cross-sectional TEM micrograph of a carbon-free wire deposited on Au/Ni electrode (b) EELS map taken along the blue arrow shown in (a).

if the samples were left in ambient air for a long time before analysis, adsorbing large amounts of carbon-based contaminants. Oxygen is likely incorporated as a result of exposure to atmospheric conditions after deposition. Finally, it should be noted that the line scan in Fig. 4(b) shows a higher Pt content in the standard Pt deposited on top of the $Pt(PF_3)_4$ precursor. However, it is important to clarify that this is ion-beam deposited Pt and thus is likely to demonstrate a higher Pt concentration anyway as a result of more efficient cracking of the Pt precursor.

To explore the origin of the carbon content in the deposits, energy dispersive x-ray (EDX) measurements were performed on both carbon-free Pt and standard Pt deposits, without breaking the chamber vacuum. As shown in Fig. S5 and Table 1 in the supporting information,[34] the EDX point scans were taken at exactly the same conditions on both the interconnect and on the nearby bare substrate to account for the carbon build-up during elemental analysis. As expected, Table 1 in the supporting information shows that the carbon content of the interconnects produced using the standard Pt precursor (C/Si ratio of 1.15 ± 0.1) was almost double that of those produced using the carbon-free Pt precursor (C/Si ratio of 0.57 ± 0.1). Furthermore, the carbon content, measured on the surface of the bare substrate (C/Si ratio of 0.45 ± 0.1) is very close to the content measured for the carbon-free Pt deposit, suggesting that the measured carbon content within the deposits obtained by the Pt $(PF_3)_4$ is solely due to the carbon build-up during the elemental analysis itself. These results also suggest that the carbon content measured by EELS shown in Fig. 4(b) could be overestimated due to the carbon build-up during analysis. Finally, although fluorine is part of the precursor molecule, its content is below the limit of detection of both EDX and EELS measurements. We speculate that fluorine, being a volatile species, is removed by vacuum during the deposition process and so was not detected during the elemental analysis.

In order to evaluate the composition of the developed Pt interconnects after N_2 annealing, EDX measurements were performed immediately after reheating the substrate on a hot plate at 120 °C for 60 min under atmospheric conditions, taking care that samples are exposed to ambient atmosphere for a very short time after reheating. Table 2 in the supporting information reveals that the absolute values of the carbon content in the standard and carbon-free precursors have increased after reheating, most probably due to excessive transient contamination form the laboratory environment. However, comparing the ratios between the standard Pt and the substrate (1.15:0.45 before annealing and 3.86:2.73 after annealing), we can see an overall decrease in C as the Si remains constant. This conclusion is based on the fact that the difference in the C/Si ratio calculated from a point measurement on the surface of the Pt deposit and on the bare substrate is less than two fold as it was measured for the samples before annealing (see Table 1, supporting information). As expected for the deposits obtained by the carbon-free Pt material, the carbon content is at similar levels both on the deposits and on the bare substrate (0.57:0.45 before annealing and 2.21:2.73 after annealing). Interestingly, we observed the formation of larger clusters [Fig. S6(a)[34]] along the length of the interconnect, which showed an increase in the phosphorous content. This is probably due to the diffusion of the amorphous material into phosphorus-containing clusters and islands by a process, which was enhanced by the thermal treatment. Note that the overall integrity of the interconnects is preserved, in contrast to the samples annealed under forming gas. Figure S6(b) is an EDX spectrum of the carbon-free interconnect shown in Fig. S6 (a).[34] Specifically, it is a point and id scan of the P cluster highlighted by the red arrow, which confirms the presence of P in the cluster. It is important to quote the melting and boiling points of elemental phosphorous (44 and 280 °C, respectively) as this may provide some insight into the annealing behavior. The 400 °C annealing temperature (discussed earlier) is well above both the melting and boiling point of phosphorus. In comparison, the 120 °C annealing step is below the boiling point and so this difference in temperatures may form the basis of a future investigation into the formation of phosphorous clusters within the carbon-free deposits. Additionally, the possible existence of volatile P-H compounds such as PH_3 (boiling point of −87.7 °C) may affect the P content of the interconnects through hydrogen contamination. This will

prove a useful study in future work, possibly providing a method to further decrease the resistivity of carbon-free Pt contacts.

Additionally, *in-situ* TEM annealing of a deposit formed from the carbon-free Pt precursor on an 80 nm thick silicon nitride membrane was performed. The deposition process on a very thin membrane differs from deposition on a substrate by the amount of deposited material due to the much lower number of secondary electrons emitted. Moreover, the interaction area of the incoming electron beam with the underlying substrate is minimised and can result in Pt structures as small as several nanometers.[39] Figure 5(a) illustrates the deposition of Pt nanoparticles on the thin silicon nitride membrane, with a size distribution similar to that obtained for the deposits on the $Au/SiO_2/Si$ substrate (the depositions are performed using the same nominal dimensions and conditions). Most importantly, the mean particle diameter for the as-deposited material of 2.7 ± 0.5 nm increases to 3.7 ± 0.7 nm after vacuum annealing at 250 °C for 10 min in the TEM (Figs. 5(b) and 5(c)]. This observation is indicative of coalescence and sintering of the Pt nanoparticles as recently investigated by aberration corrected STEM at room temperature.[40] Theoretical studies predict an increased rate of sintering for nanoscale metal particles in comparison to micron-sized metal powders.[41–43] Furthermore, experimental results demonstrate that metal nanoparticles sinter at temperatures far lower than those predicted from conventional scaling models.[44,45] Here, we observe Pt nanoparticles sintering at temperatures as low as 250 °C.

Most significantly, the obtained *in-situ* annealing data, together with the elemental analysis before and after N_2 annealing, are important in understanding the decreased resistivity of the interconnects after annealing and the obtained high break-down currents. Increased conductivity of several orders of magnitude in ink-jet printed nanoparticulate Ag interconnects has been attributed to increased particle size by electrical sintering.[46] Similarly, our interconnects increase their conductivity by applying higher potential until break-down at which point the interconnect is transformed into large isolated islands of Pt. This behavior is likely due to localized Joule heating. A method for determining the spatial distribution of the temperature gradients due to Joule heating around a metal-containing interconnect on a silicon nitride membrane has been demonstrated.[47] Their results indicated the formation of larger metallic nanoparticles as a function of the applied electrical power. Our results suggest that the Pt interconnects developed from the carbon-free precursor show improved performance after N_2 annealing mainly due to nanoparticle sintering, improved crystallinity, and locally minimized amorphous impurities.

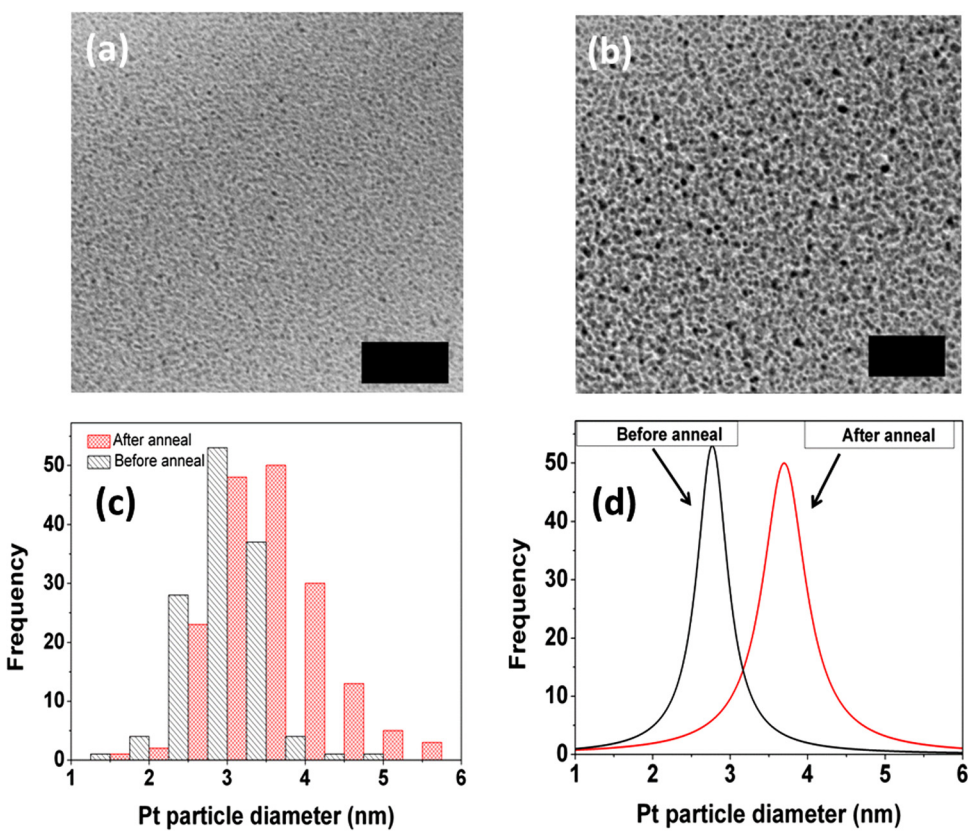

FIG. 5. (Color online) Transmission electron micrographs and diameter distributions of platinum particles deposited using $Pt(PF_3)_4$. (a) TEM micrograph of Pt particles before *in-situ* TEM annealing at 250 °C. (b) TEM micrograph of Pt particles after *in-situ* TEM annealing at 250 °C. Scale bars in (a) and (b) are 50 nm. (c) Diameter distribution of Pt particles before and after annealing. The distribution shows a clear increase in particle size after annealing, suggesting the sintering of particles together which can be correlated to the decrease in resistivity after annealing. (d) Lorentzian fit to the distribution in (c), which highlights the difference in particle sizes more clearly.

IV. SUMMARY AND CONCLUSIONS

Pt interconnects deposited from the carbon-free precursor, $Pt(PF_3)_4$, using EBID demonstrated very low resistivities compared to interconnects produced using a standard Pt precursor. After devising two different annealing procedures and measuring the "true" cross-sectional area of the interconnects, we demonstrate that low resistivity Pt interconnects showing resistivities of about 0.24×10^{-3} Ω cm and 0.2 Ω cm can be obtained for the carbon-free and standard precursors, respectively. A maximum current density (J_{max}) of 1.87×10^7 A cm^{-2} was achieved for the $Pt(PF_3)_4$ precursor. This was 2 orders of magnitude higher than the maximum current density achieved for the standard $(CH_3)_3Pt(C_pCH_3)$ precursor. Additionally, the enhanced electrical properties of the as-deposited carbon-free Pt materials are explained by the absence of large amounts of carbon impurities, and their further improvement by postdeposition annealing under inert gases. N_2 annealing of these interconnects proved very effective at lowering their resistivity. In comparison interconnects formed from the standard Pt precursor demonstrated an improvement in resistivity of 2 orders of magnitude after annealing in forming gas. Our *in-situ* TEM results and elemental composition studies suggest that the Pt interconnects developed from the carbon-free precursor show improved performance after N_2 annealing mainly due to nanoparticle sintering, improved crystallinity, and locally minimized amorphous impurities. Due to the higher current density and lower resistivity of Pt interconnects formed from the carbon-free Pt precursor, in comparison to the structures formed from the standard Pt precursor, $Pt(PF_3)_4$ is likely to become a preferred precursor for EBID deposition of Pt metal for fast and effective prototyping of devices.

ACKNOWLEDGMENTS

The authors acknowledge financial support from the Irish Research Council and Science Foundation Ireland (Grant Nos.: 09/SIRG/I1621 and 09/IN.1/I2602). This research was also enabled by the Higher Education Authority Program for Research in Third Level Institutions (2007-2011) via the INSPIRE programme. The authors would also like to thank Karim Cherkaoui of Tyndall National Institute for useful discussions.

[1]A. M. Contreras, J. Grunes, X. Yan, A. Liddle, and G. Somorjai, Catal. Lett. **100**, 115 (2005).
[2]D. Drouin, J. Beauvais, R. Lemire, E. Lavallée, R. Gauvin, and M. Caron, Appl. Phys. Lett. **70**, 3020 (1997).
[3]S. Jin, D. Whang, M. C. McAlpine, R. S. Friedman, Y. Wu, and C. M. Lieber, Nano Lett. **4**, 915 (2004).
[4]V. Gopal, V. R. Radmilovic, C. Daraio, S. Jin, P. Yang, and E. A. Stach, Nano Lett. **4**, 2059 (2004).
[5]D. Wang, Q. Wang, A. Javey, R. Tu, H. Dai, H. Kim, P. C. McIntyre, T. Krishnamohan, and K. C. Saraswat, Appl. Phys. Lett. **83**, 2432 (2003).
[6]L. Zhang, R. Tu, and H. J. Dai, Nano Lett. **6**, 2785 (2006).
[7]J. Andzane, N. Petkov, A. I. Livshits, J. J. Boland, J. D. Holmes, and D. Erts, Nano Lett. **9**, 1824 (2009).
[8]K. J. Ziegler, D. M. Lyons, J. D. Holmes, D. Erts, B. Polyakov, H. Olin, K. Svensson, and E. Olsson, Appl. Phys. Lett. **84**, 4074 (2004).
[9]P. Kim and C. M. Lieber, Science **286**, 2148 (1999).
[10]J. M. Kinaret, T. Nord, and S. Viefers, Appl. Phys. Lett. **82**, 1287 (2003).
[11]L. Mazeina, F. K. Perkins, V. M. Bermudez, S. P. Arnold, and S. M. Prokes, Langmuir **26**, 13722 (2010).
[12]D. C. Arnold, R. G. Hobbs, M. Zirngast, C. Marschner, J. J. Hill, K. J. Ziegler, M. A. Morris, and J. D. Holmes, J. Mater. Chem. **19**, 954 (2009).
[13]T. Cacouris, R. R. Krchnavek, H. H. Gilgen, R. M. Osgood, Jr., S. Kulick, and J. Schoen, *Laser Direct Writing of Metal Interconnects* (IEEE, New York, 1985), p. 594.
[14]N. Silvis-Cividjian, C. W. Hagen, P. Kruit, M. A. J. vd Stam, and H. B. Groen, Appl. Phys. Lett. **82**, 3514 (2003).
[15]A. Botman, J. J. L. Mulders, R. Weemaes, and S. Mentink, Nanotechnology **17**, 3779 (2006).
[16]I. Utke, P. Hoffmann, B. Dwir, K. Leifer, E. Kapon, and P. Doppelt, J. Vac. Sci. Technol. B **18**, 3168 (2000).
[17]C. Y. Nam, J. Y. Kim, and J. E. Fischer, Appl. Phys. Lett. **86**, 193112 (2005).
[18]T. Tao, J. S. Ro, J. Melngailis, Z. Xue, and H. D. Kaesz, J. Vac. Sci. Technol. B **8**, 1826 (1990).
[19]S. B. Cronin, Y. M. Lin, O. Rabin, M. R. Black, J. Y. Ying, M. S. Dresselhaus, P. L. Gai, J. P. Minet, and J. P. Issi, Nanotechnology **13**, 653 (2002).
[20]C. Y. Ho, S. H. Chiu, J. J. Ke, K. T. Tsai, Y. A. Dai, J. H. Hsu, M. L. Chang, and J. H. He, Nanotechnology **21**, 134008 (2010).
[21]C. Vieu, F. Carcenac, A. Pepin, Y. Chen, M. Mejias, A. Lebib, L. Manin-Ferlazzo, L. Couraud, and H. Launois, Appl. Surf. Sci. **164**, 111 (2000).
[22]A. I. Hochbaum, R. Chen, R. D. Delgado, W. Liang, E. C. Garnett, M. Najarian, A. Majumdar, and P. Yang, Nature **451**, 163 (2008).
[23]C. Qi, G. Goncher, R. Solanki, and J. Jordan, Nanotechnology **18**, 075302 (2007).
[24]J. H. He, P. H. Chang, C. Y. Chen, and K. T. Tsai, Nanotechnology **20**, 135701 (2009).
[25]C. Y. Nam, D. Tham, and J. E. Fischer, Nano Lett. **5**, 2029 (2005).
[26]T. Hanrath and B. A. Korgel, Proc. IME, Part N **218**, 25 (2004).
[27]K. Thompson, D. Lawrence, D. J. Larson, J. D. Olson, T. F. Kelly, and B. Gorman, Ultramicroscopy **107**, 131 (2007).
[28]M. H. Ervin, D. Chang, B. Nichols, A. Wickenden, J. Barry, and J. Melngailis, J. Vac. Sci. Technol. B **25**, 2250 (2007).
[29]M. Allan, J. Chem. Phys. **134**, 204309 (2011).
[30]M. Takeguchi, M. Shimojo, and K. Furuya, Appl. Phys. A **93**, 439 (2008).
[31]A. Botman, M. Hesselberth, and J. J. L. Mulders, J. Vac. Sci. Technol. B. **26**, 2464 (2008).
[32]L. A. Giannuzzi and F. A. Stevie, Micron **30**, 197 (1999).
[33]R. J. Dias, C. O'Regan, P. Thrompenaars, A. Romano-Rodriguez, J. D. Holmes, J. J. L. H. Mulder, and N. Petkov, J. Phys.: Conf. Ser. **371**, 012038 (2012).
[34]See supplementary material at http://dx.doi.org/10.1116/1.4794343 for additional information and data including 2 and 4-point measurements of the carbon-free interconnect, additional 2-point measurements for both precursors before and after annealing under forming gas, EDX analysis of the interconnect composition and a TEM cross-section image detailing the difference between the actual and nominal cross-section values.
[35]J. D. Barry, M. Ervin, J. Molstad, A. Wickenden, T. Brintlinger, P. Hoffman, and J. Meingailis, J. Vac. Sci. Technol B **24**, 3165 (2006).
[36]Y. C. Lin, K. C. Lu, W. W. Wu, J. Bai, L. J. Chen, K. N. Tu, and Y. Huang, Nano Lett. **8**, 913 (2008).
[37]Y. Wu, J. Xiang, C. Yang, W. Lu, and C. M. Lieber, Nature **430**, 61 (2004).
[38]C. Y. Kang, C. H. Chao, S. C. Shiu, L. J. Chou, M. T. Chang, G. R. Lin, and C. F. Lin, J. Appl. Phys. **102**, 073508 (2007).
[39]W. F. van Dorp, B. van Someren, C. W. Hagen, P. Kruit, and P. A. Crozier, Nano Lett. **5**, 1303 (2005).
[40]M. A. Asoro, D. Kovar, Y. Shao-Horn, L. F. Allard, and P. J. Ferreira, Nanotechnology **21**, 025701 (2010).
[41]C. Herring, J. Appl. Phys. **21**, 301 (1950).
[42]R. L. Coble, J. Am. Ceram. Soc. **41**, 55 (1958).
[43]W. D. Kingery and M. Berg, J. Appl. Phys. **26**, 1205 (1955).
[44]J. R. Groza, Nanostruct. Mater. **12**, 987 (1999).
[45]Y. Champion, F. Bernard, N. Guigue-Millot, and P. Perriat, Mater. Sci. Eng., A **360**, 258 (2003).
[46]M. L. Allen, M. Aronniemi, T. Mattila, A. Alastalo, K. Ojanperä, M. Suhonen, and H. Seppä, Nanotechnology **19**, 175201 (2008).
[47]A. Reguer, F. Bedu, S. Nitsche, D. Chaudanson, B. Detailleur, and H. Dallaporta, Ultramicroscopy **110**, 61 (2009).